ORIGINAL RESEARCH ARTICLE

Crystallization Behaviors of CaF_2–CaO–Al_2O_3–MgO–B_2O_3 Slag for Electroslag Remelting of B-Containing Rack Steel

YONG-JIAO ZHANG, XI-MIN ZANG, LING-ZHONG KONG, JIE YANG, SHI-SEN LI, and GUO-CHENG WANG

The crystallization behaviors of CaF_2–CaO–Al_2O_3–MgO–B_2O_3 slag for electroslag remelting of B-containing rack steel was investigated through a series of non-isothermal and isothermal crystallization experiments. The techniques employed for this determination included differential scanning calorimetry, X-ray diffraction, scanning electron microscopy-energy dispersive spectroscopy, and FactSage 8.2. The results indicated that an increase in B_2O_3 content suppressed the crystallization of CaF_2–CaO–Al_2O_3–MgO slag. The crystallization temperature decreased as the B_2O_3 content in the slag increased from 2 to 7 mass pct. In the slag containing 2 mass pct B_2O_3, spherical CaF_2 precipitates first, followed by reticulate $Ca_{12}Al_{14}F_2O_{32}$ phase. Increasing B_2O_3 addition promoted the formation of $Ca_5(BO_3)_3F$ and calcium aluminate ($Ca_{12}Al_{14}O_{33}$ or $CaAl_4O_7$), and decreased the crystallization of $Ca_{12}Al_{14}F_2O_{32}$ phase. The crystallization sequence transformed into $CaF_2 \rightarrow CaAl_4O_7 \rightarrow MgAl_2O_4 + Ca_5(BO_3)_3F$ in the case of 7 mass pct B_2O_3. B_2O_3 addition inhibits the crystallization of the dominated phase CaF_2, which would improving the lubrication and heat transfer performance of ESR-type CaF_2–CaO–Al_2O_3–MgO slags.

https://doi.org/10.1007/s11663-024-03243-7

I. INTRODUCTION

RACK steel containing boron (B) plays a crucial role in the exploitation of deep-sea oil and gas resources in marine engineering.[1,2] As deep-sea exploration goes deeper, there is an urgent need for larger-scale rack steel plates. However, some defects such as porosity, segregation, and crack would be prone to occur if the traditional process (continuous casting or die casting) is applied. Due to the uniform structure and good surface quality of electroslag remelting ingots, electroslag remelting (ESR) is commonly used to produce large-scale rack steel plates.[3] But, the element B in the steel will be oxidized during the ESR process of rack steel, which significantly compromises the mechanical properties of the rack steel.[4,5] The loss of B in the steel is primarily attributed to the steel–slag reactions. Previous studies[6,7] have shown that the addition of B_2O_3 to the slag can effectively mitigate the loss of B in the steel.

It is widely acknowledged that the composition of slag has a significant impact on its physical and chemical properties.[8–10] As one of the most important properties of slag, the crystallization performance of slag has an important impact on the surface quality of the electroslag ingot, the heat transfer of the mold, and the friction between the slag shell and the steel shell (in the drawing-ingot-type electroslag remelting).[11] Consequently, numerous researchers have conducted studies to investigate the impact of ESR slag composition on the crystallization behaviors of the slag. Shi *et al.*[12] found that adding an appropriate amount of SiO_2 to CaF_2–CaO–Al_2O_3 slag could provide better lubrication and heat transfer. Liu *et al.*[13] discovered that SiO_2 could enhance the polymerization degree of the CaF_2–CaO–Al_2O_3 slag, thereby reducing the crystallization temperature and amount of primary crystals in the slag. Zheng *et al.*[14] believed that the presence of TiO_2 in the ESR slag could lower its crystallization temperature and inhibit its crystallization tendency. Ju *et al.*[15] observed that the types and sequence of crystalline phases remained unchanged even when the TiO_2 content

YONG-JIAO ZHANG, LING-ZHONG KONG, JIE YANG, SHI-SEN LI, and GUO-CHENG WANG are with the School of Materials and Metallurgy, University of Science and Technology Liaoning, Anshan 114051, Liaoning, P.R. China. Contact e-mail: klz_0110@163.com, jierui1120@163.com XI-MIN ZANG is with the School of Materials Science and Engineering, Shenyang University of Technology, Shenyang 110870, Liaoning, P.R. China. Contact e-mail: zangxm@sut.edu.cn

Manuscript submitted December 24, 2023; accepted August 6, 2024.

Published online: 14 August 2024

increased to 13 mass pct in the low-fluorine slag. However, limited studies have been conducted to reveal the effect of B_2O_3 on the crystallization behaviors of ESR slag. Huang *et al.*[16] reported that increasing B_2O_3 addition from 0 to 3.2 mass pct lowered the crystallization temperature of CaF_2–CaO–Al_2O_3 slag. Peng *et al.*[17] suggested that the crystallization order was $CaF_2 \rightarrow MgO$ and/or $MgAl_2O_4 \rightarrow Ca_3B_2O_6$ during the cooling process of CaF_2–CaO–Al_2O_3 slag with less than 3 mass pct B_2O_3 slag. Nevertheless, the crystallization mechanism of B_2O_3 in CaF_2–CaO–Al_2O_3 slag remains elusive. Furthermore, it cannot be guaranteed that B in the rack steel (approximately 0.0012 mass pct) will not burnout during the ESR process when employing slag containing 3 mass pct B_2O_3. To minimize the loss of titanium in Ti-containing steels, the slags containing 9 mass pct TiO_2 are considered to apply in ESR production.[18] Similarly, to inhibit the loss of B in rack steel, it is imperative to investigate the crystallization behaviors of slag with higher B_2O_3 content.

The crystallization behaviors of CaF_2–CaO–Al_2O_3 slag with varying B_2O_3 (2 to 7 mass pct) were intensively studied in the current paper. The differential scanning calorimetry (DSC, Netzsch, STA449F3, Germany) was used to investigate the non-isothermal crystallization process of the B_2O_3-bearing ESR slag. The compositions and morphology of the crystalline phases were analyzed by X-ray diffraction (XRD, D8 ADVANCE, Bruker, Germany), scanning electron microscopy-energy dispersive spectroscopy (SEM–EDS, FEI Apreos, Hillsboro), and FactSage 8.2. Additionally, the impact of B_2O_3 on the crystallization rate of the slag was assessed based on crystallization kinetics analysis. The transformation of the crystallization characteristics of the B_2O_3-containing ESR slag found in the study provides valuable insights for the development of B_2O_3-bearing ESR slag for rack steel.

II. EXPERIMENTAL

A. *Sample Preparation*

Reagent-grade powders of CaF_2, CaO, Al_2O_3, MgO, and B_2O_3 were used to prepare pre-melting slag. To eliminate any potential moisture and carbonate, the CaO powder was baked at 1050 °C (1323 K) for 8 hours prior to use. According to author's previous result,[19] a composition of 50.48 mass pct CaF_2–24.81 mass pct CaO–24.71 mass pct Al_2O_3 was employed in this paper. Table I provides the detailed compositions of the experimental slags. The mixed powder was poured into a graphite crucible (Φ60 mm×130 mm) lined with a 0.2-mm-thick molybdenum film. Subsequently, the graphite crucible was placed inside a $MoSi_2$ furnace at 1500 °C (1773 K) for 1 hour to ensure completely melting and homogenization of the slag. The liquid slag was rapidly quenched in iced water and then dried in a muffle furnace. Finally, the dried pre-melting slag was crushed and ground. Throughout the experiments, High-purity Ar gas (purity 99.999 mass pct) was introduced into the furnace.

B. *DSC Measurement*

DSC was utilized to confirmed the non-isothermal crystallization behaviors of pre-melting slags. The temperature and heat flow of the instrument were calibrated using the heat flux method. Approximately 30 mg of the pre-melting slag power was placed in a platinum crucible (Φ6.7 mm × 4 mm). Another same platinum crucible served as a reference. The measurements were conducted in an argon atmosphere with a flow rate of 60 $mL \cdot min^{-1}$. The slag power was heated from room temperature to 1500 °C (1773 K) with the heating rate of 30 $°C \cdot min^{-1}$, followed by cooling to 350 °C (623 K) with a constant cooling rate (15 or 25 $°C \cdot min^{-1}$). Throughout the measurement process, the DSC data were automatically recorded. Furthermore, a baseline was incorporated to calibrate the DSC curve and minimize the influence of gas flow.

C. *XRD and SEM–EDS Analysis*

To determine the crystalline phase of the slag, isothermal crystallization experiments were carried out. The pre-melting slag power was placed in a graphite crucible (Φ21 mm × 60 mm) and heated in $MoSi_2$ furnace at 1500 °C (1773 K) for 30 minutes. Subsequently, the melting slag was cooled to a specific temperature with the rate of 15 $°C \cdot min^{-1}$. To obtain the first-crystalline phase of the slag samples, the samples were held for 10 minutes at the temperature below the starting crystallization temperature of the first exothermic peak on the DSC curve with the rate of 15 $°C \cdot min^{-1}$. Therefore, the first-crystalline phase in the slags was fully crystallized at the end crystallization temperature. However, it should be noted that long holding time may promote isothermal crystallization, so the holding time should not be too long. The molten slag was subsequently quenched in ice water to preserve its high-temperature structure. The same procedure was

Table I. The Composition of the Experimental Slags (Mass Pct)

	Before Pre-melted					After Pre-melted				
Slags Nos.	CaF_2	CaO	Al_2O_3	MgO	B_2O_3	CaF_2	CaO	Al_2O_3	MgO	B_2O_3
1#	48.46	23.82	23.72	2	2.00	47.96	24.31	23.71	2.08	1.94
2#	47.96	23.57	23.47	2	3.00	46.95	24.58	23.52	2.06	2.89
3#	46.95	23.07	22.98	2	5.00	45.99	24.14	22.97	2.05	4.85
4#	45.94	22.58	22.49	2	7.00	44.83	23.54	22.81	2.03	6.79

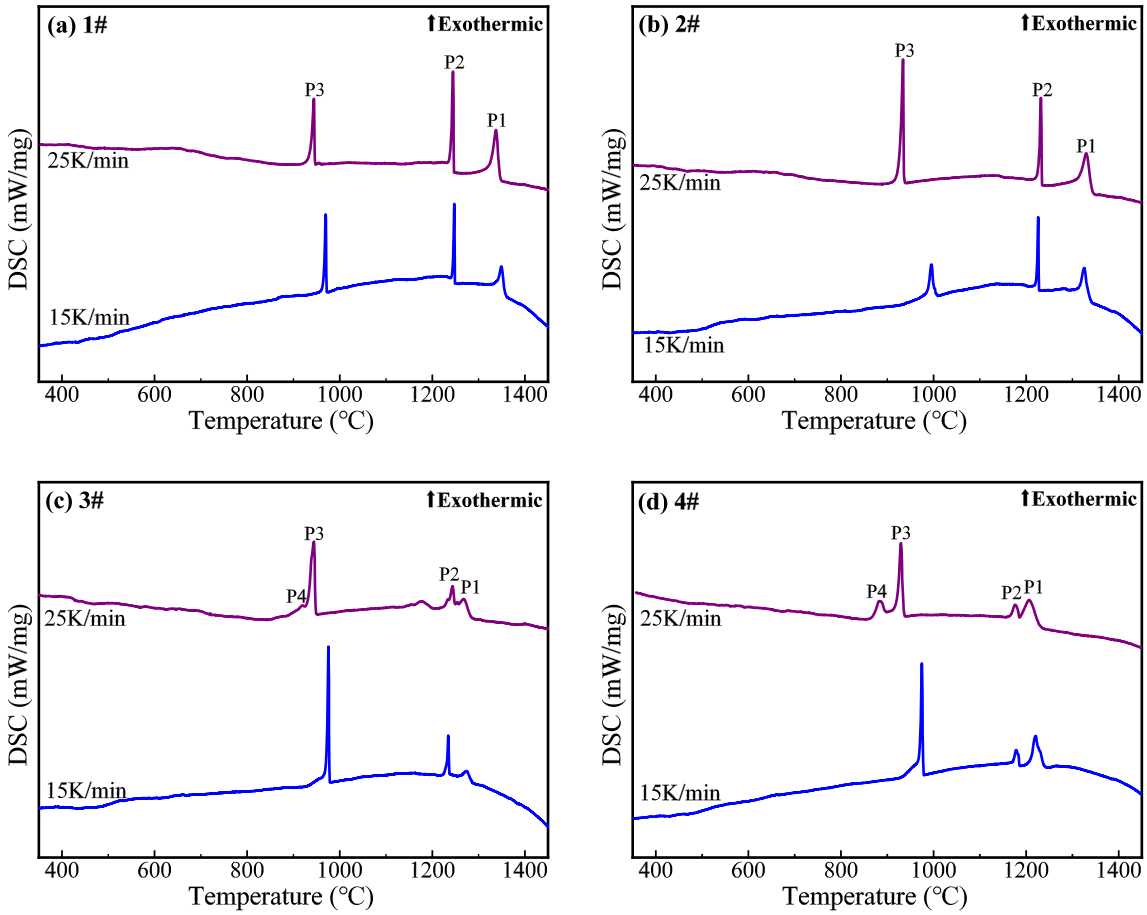

Fig. 1—The DSC curves of experimental slags at various cooling rates: (*a*) slag 1#: $w(B_2O_3)$ = 2 mass pct, (*b*) slag 2#: $w(B_2O_3)$ = 3 mass pct, (*c*) slag 3#: $w(B_2O_3)$ = 5 mass pct, and (*d*) slag 4#: $w(B_2O_3)$ = 7 mass pct.

followed to obtain other crystalline phases. Previous studies[14,15,20] have shown that reducing the cooling rate results in an increase the crystallization temperature of crystalline phases. Then, XRD analysis was employed to examine the crystalline phases of the quenched slags, while SEM–EDS was utilized to identify the morphology of the crystalline phases.

D. *Thermodynamic Calculation*

The phase equilibrium of the slag was calculated by FactSage 8.2. It should be noted that once solid phase precipitation occurs during the cooling process of the slag, it no longer participates in subsequent solid–liquid equilibrium reactions or reactions between solid phases.[21,22] Therefore, for the non-equilibrium calculation, the Scheil–Gulliver cooling conditions in FactSage 8.2 were utilized. This model is widely employed in studies related to solidification at high cooling rate.[23–25] The FToxid database was selected for the calculation. The calculated temperature range was from 1500 °C (1623 K) to 650 °C (923 K) with a step of 5 °C. The Scheil–Gulliver cooling mode is selected for cooling conditions. The calculation results were compared to the experiment results of slag to gain insights into the crystallization behaviors of B_2O_3-bearing ESR slag.

E. *Relative Crystallinity*

Relative crystallinity is an important parameter to study the crystallization kinetics. According to the definition of relative crystallinity, its calculation formula can be obtained as follows[26–28]:

$$C(T) = \frac{\int_{T_0}^{T_i} (\mathrm{d}H_c/\mathrm{d}T)\mathrm{d}T}{\int_{T_0}^{T_F} (\mathrm{d}H_c/\mathrm{d}T)\mathrm{d}T}. \quad [1]$$

In the formula, T_i is a certain temperature in the crystallization process, K; T_0 is the starting temperature of the exothermic peak, K; T_F is the end temperature of the exothermic peak, K; and $\mathrm{d}H_c$ is the crystallization enthalpy under the infinitesimal $\mathrm{d}T$ in the crystallization process, kJ mol^{-1}.

III. RESULTS AND DISCUSSION

A. *Crystallization Temperature of Crystalline Phases*

The DSC curves of the CaF_2–CaO–Al_2O_3–MgO–x mass pct B_2O_3 slag with varying cooling rates (15 and 20 °C·min^{-1}) are illustrated in Figure 1. In the figure, the exothermic peaks on the DSC curves were denoted as P1, P2, P3, and P4 in sequential order. It is noteworthy

Table II. The Temperature of Exothermic Peak on DSC Curve (°C)

	Sample Nos.	1#		2#		3#		4#	
	Rate of cooling (°C·min^{-1})	15	25	15	25	15	25	15	25
P1	starting temperature	1357	1346	1335	1343	1287	1284	1230	1229
	peak temperature	1349	1338	1326	1330	1274	1268	1220	1207
	end temperature	1341	1325	1316	1315	1264	1258	1210	1187
P2	starting temperature	1249	1247	1228	1234	1237	1248	1186	1185
	peak temperature	1248	1245	1226	1232	1235	1244	1178	1177
	end temperature	1239	1231	1216	1217	1231	1225	1172	1167
P3	starting temperature	972	946	1001	936	978	948	978	935
	peak temperature	967	944	996	934	976	944	975	930
	end temperature	966	918	988	905	972	931	971	922
P4	starting temperature	—	—	—	—	—	931	—	894
	peak temperature	—	—	—	—	—	919	—	882
	end temperature	—	—	—	—	—	884	—	868

that DSC curves of the slags exhibit three exothermic peaks from 1450 °C (1723 K) to 350 °C (623 K), except for the slags 3# and 4# obtained at a cooling rate of 25 °C·min^{-1}. The presence of P4 could represent either a new crystallization event or an independent exothermic peak separated from P3. The definitive conclusions would be drawn based on subsequent analysis using XRD and SEM–EDS. On the contrary, the intensity of P1 and P2 in Figures 1(c) and (d) was lower than those in Figures 1(a) and (b), which means a weaker crystallinity for P1 and P2.[29] Additionally, P1 becomes connected with P2 when B_2O_3 content ranged from 5 to 7 mass pct. It is noteworthy that the DSC results of CaF_2–CaO–Al_2O_3–MgO–B_2O_3 slag by Peng *et al.*[17] and Huang *et al.*[16] exhibit similarities to the findings of this research, with three exothermic peaks observed.

The DSC curves provide valuable information about the crystallization events in the slag. The onset temperature and finish temperature of an exothermic peak in the DSC curves correspond to the starting temperature and ending temperature of the crystallization event, respectively.[4] Furthermore, the peak temperature of the exothermic peak represents the maximum heat release temperature. To summarize the crystallization temperatures of all the crystalline phases in the slags, refer to Table II.

Based on Table II, the continuous cooling transformation (CCT) curves of the experimental slag were obtained and are presented in Figure 2. It can be observed that as the cooling rate of the slag decreases from 25 to 15 °C·min^{-1}, the starting crystallization temperatures of the first- and second-crystalline phases remain relatively constant, while the crystallization temperature of the third-crystalline phase (shown in Figure 2(c)) significantly increases. This suggests that the third-crystalline phase requires less undercooling for nucleation with a lower cooling rate, indicating an enhanced crystallization ability of the ESR slag. Similar findings were reported by Shi *et al.*[30] and Lin *et al.*,[31] who observed a decrease in the crystallization temperature of crystalline phases with increasing cooling rates. On the other hand, decreasing cooling rate of the slag narrows the crystallization temperature range of all crystalline phases. For example, for slag 1#, the range of crystallization temperature of the first-crystalline phase decreased from 21 °C (from 1346 °C to 1325 °C) to 16 °C (from 1357 °C to 1341 °C) as the cooling rate dropped from 25 to 15 °C·min^{-1}. Shi *et al.*[12] found the similar results in the CaO–Al_2O_3-based mold flux. Figure 2 also illustrates the relationship between the B_2O_3 content in the slag and the starting crystallization temperatures of the different crystal phases. As the B_2O_3 content increases, the starting crystallization temperature of P1 decreases significantly, and the starting crystallization temperature of P2 shows a slight decrease, and the initial crystallization temperature of P3 remains relatively constant. Wei *et al.*[32] suggested that the decrease of crystallization temperature was related to the polymerization degree of the slag. Moreover, Huang *et al.*[16] also noted that the weakening of ESR slag crystallization with B_2O_3 addition might be attributed to the increase of polymerization degree of slag and growing the diffusion resistance of slag components in the slag. Therefore, a greater undercooling is required for the slag to generate a stronger driving force for crystallization to overcome the increased crystallization resistance. It was worth noting that, the first-crystalline phase with most precipitation amount was significantly influenced by the structure of the slag. However, the third-crystalline phase with least precipitation amount was minimally affected by the slag structure. This is because the starting crystallization temperatures of P2 and P3 are lower than P1 (as shown in Figure 1), which caused a large diffusion resistance for slag components. Consequently, the increased B_2O_3 content did not significantly reduce the crystallization

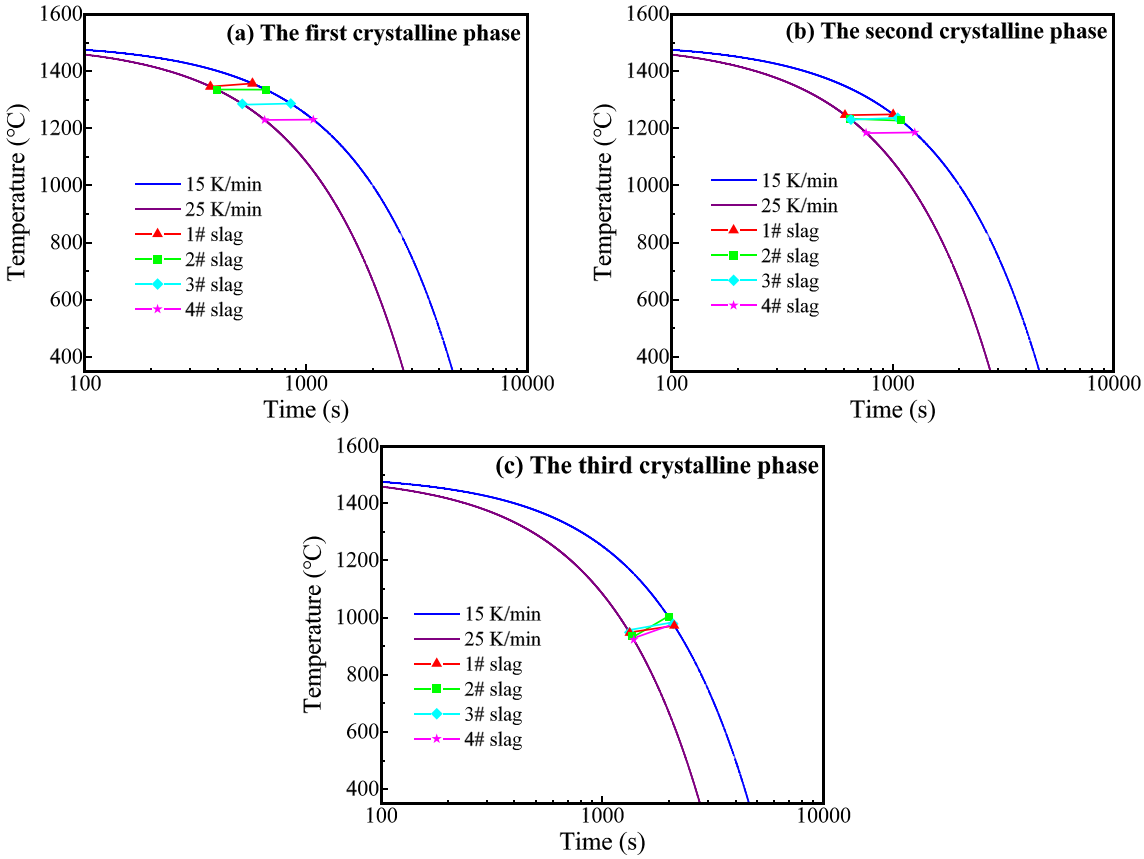

Fig. 2—The CCT diagram of crystalline phases in the slags: (*a*) the first-crystalline phase, (*b*) the second-crystalline phase, and (*c*) the third-crystalline phase.

temperature of the P2 and P3. Liu *et al.*[13] reported the similar behavior in the crystallization of CaF_2–CaO–Al_2O_3–(SiO_2) slag. Lower crystallization temperature can provide thin slag skin and stable heat transfer, which is beneficial to improve the surface quality of ESR ingot.[33,34]

The crystallization characteristics of the molten slag play a crucial role in the horizontal heat transfer between the solidifying steel shell and the mold. One significant parameter that affects crystallization performance is the crystallization temperature, which is related to the formation of surface defects on the cast ingot. It is important to note that the slag film that forms between the solidifying steel shell and the copper mold consists of both a solid layer and a liquid layer.[35–37] During the ESR process, molten slag with lower crystallization temperature will generate a thinner solid layer. Firstly, the thinner solid layer reduces the friction between the slag film and the steel ingot.[38] Additionally, the thinner solid layer enhances the heat flux across the slag film and improves the strength of initially solidifying steel shell.[33] In conclusion, increasing the B_2O_3 content in the slag is advantageous for reducing the crystallization temperature. This improvement enhances surface quality of the cast ingot, reducing the occurrence of surface defects such as ripples, bleed, and slag runner.[39,40]

B. *Components of Crystalline Phases*

The XRD analysis of the four slags quenched at the end temperature of exothermic peaks on DSC curve with the cooling rate of 15 °C·min^{-1} is presented in Figure 3. Since the slags 3# and 4# had P4 on the DSC curve of the 25 °C·min^{-1} cooling rate, XRD analysis was also performed on the quenched slag at the end temperature of the P4. The XRD results are summarized in Table III. The phase identification was based on the ICSD patterns of CaF_2 (PDF 75-0363), $Ca_{12}Al_{14}F_2O_{32}$ (PDF 36-0678), $MgAl_2O_4$ (PDF 77-1193), $Ca_{12}Al_{14}O_{33}$ (PDF 70-2144), $CaAl_4O_7$ (PDF 23-1037), and $Ca_5(BO_3)_3F$ (PDF 79-0803).

Figure 3(a) is the XRD patterns of the slag 1# contain 2 mass pct B_2O_3. The XRD analysis revealed that the first-crystalline phase in slag 1# corresponded to CaF_2 phase. And the P2 represented the precipitation of $Ca_{12}Al_{14}F_2O_{32}$, while in slag 1#, no new phase was precipitated at the P3 which may be because the precipitation amount of the $MgAl_2O_4$ below the detection limit of XRD.[41]

Figure 3(b) is the XRD patterns of the slag 2# contain 3 mass pct B_2O_3. It was confirmed from the XRD patterns that the P1 and the P2 represented CaF_2 and $Ca_{12}Al_{14}F_2O_{32}$ crystals formation, respectively. The XRD analysis revealed that the P3 on DSC curves of slag 2# corresponded to $MgAl_2O_4$ phase.

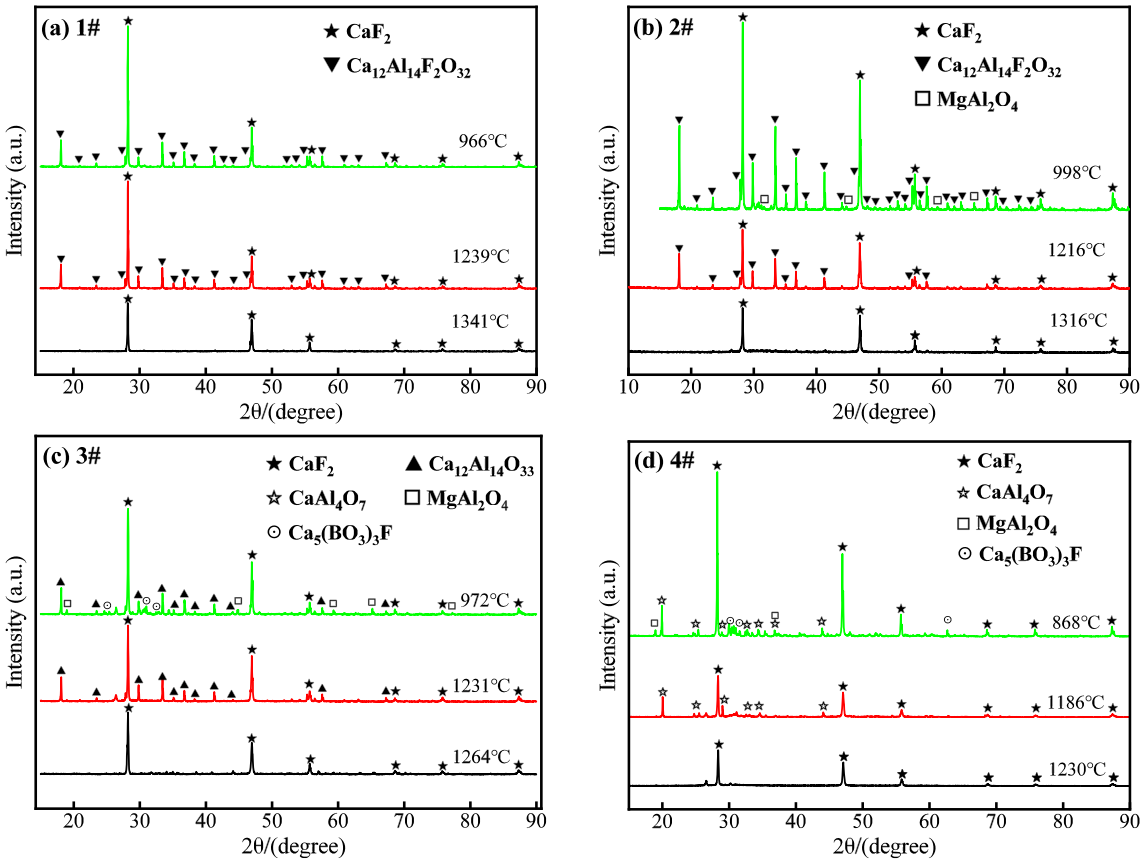

Fig. 3—XRD analysis of the current slags: (*a*) slag 1#: $w(B_2O_3)$ = 2 mass pct, (*b*) slag 2#: $w(B_2O_3)$ = 3 mass pct, (*c*) slag 3#: $w(B_2O_3)$ = 5 mass pct, and (*d*) slag 4#: $w(B_2O_3)$ = 7 mass pct.

Figure 3(c) is the XRD patterns of the slag 3# contain 5 mass pct B_2O_3. The XRD analysis confirmed that P1 occurred in slag 2# during continuous cooling corresponded to the crystallization of CaF_2 phase. The P2 represented the crystallization of $Ca_{12}Al_{14}O_{33}$ phase. And the P3 was identified as simultaneous precipitation of $Ca_5(BO_3)_3F$ phase and $MgAl_2O_4$ phase precipitated. Notably, there was a small exothermic peak of P4 near the end temperature of the P3 peak in Figure 1(c). Because the P3 and P4 partially overlapped, it was difficult for XRD analysis to identify the precipitation order of the two crystallization phases.

Figure 3(d) is the XRD patterns of the slag 4# contain 7 mass pct B_2O_3. It was confirmed from the XRD patterns that the P1 and the P2 represented CaF_2 and $CaAl_4O_7$ phases formation, respectively. The crystalline phases in the sample quenched at 868 °C (1142 K) were $MgAl_2O_4$ phase and $Ca_5(BO_3)_3F$ phase, respectively. The overlap of P4 and P3 (as shown in Figure 1(d)) makes it difficult to detect the precipitation sequence of $MgAl_2O_4$ phase and $Ca_5(BO_3)_3F$ phase.

The appearance of the P4 in slags 3# and 4# may be related to the increase of B_2O_3 addition in the slags. The increase of B_2O_3 addition promoted the formation of $Ca_5(BO_3)_3F$ by increasing the activity of B_2O_3 in the slags. CaF_2 and CaO in the slag are bound by B_2O_3, resulting the P2 crystalline phase $Ca_{12}Al_{14}F_2O_{32}$ containing CaF_2 and CaO gradually transforms to $Ca_{12}Al_{14}O_{33}$ or $CaAl_4O_7$.

The order of crystal precipitation during the cooling process of slag 1# can be observed in Figure 3 (a) which is $CaF_2 \rightarrow Ca_{12}Al_{14}F_2O_{32}$. As B_2O_3 increased, $MgAl_2O_4$ phase and $Ca_5(BO_3)_3F$ phase began to precipitate significantly, and $Ca_{12}Al_{14}F_2O_{32}$ phase was gradually replaced by $Ca_{12}Al_{14}O_{33}$ or $CaAl_4O_7$ phase. Figure 3(d) shown that the crystallization sequence of slag 4# was $CaF_2 \rightarrow CaAl_4O_7 \rightarrow MgAl_2O_4 + Ca_5(BO_3)_3F$. The B_2O_3 addition increased the activity of B_2O_3, so $Ca_5(BO_3)_3F$ was easier to generated. Subsequently, the crystallization of $Ca_{12}Al_{14}F_2O_{32}$ phase containing CaF_2 was inhibited. These observations will be further confirmed by the SEM–EDS analysis of the crystalline phases in Section III–C. To confirm the accuracy of XRD analysis of slag 4#, two additional groups of slags with higher B_2O_3 content (9 mass pct and 11 mass pct) were included to determine the crystalline phases of B_2O_3-containing ESR slag. (The composition of additional slags is provided in Electronic Supplementary Table S1, and their XRD results are displayed in Electronic Supplementary Figure S1). It is evident that $Ca_5(BO_3)_3F$ was observed in slag with higher B_2O_3 content, which indicating a significant transformation in the crystalline phase type when the B_2O_3 in the slag increases to 7 mass pct.

Table III. XRD Analysis Results of Crystalline Phases Present in the ESR Slags Quenched at the Desired Target Temperatures

Label	Target Temperature (°C)	Crystalline Phases Identified by XRD
1#	1341	CaF_2
	1239	CaF_2 + $Ca_{12}Al_{14}F_2O_{32}$
	966	CaF_2 + $Ca_{12}Al_{14}F_2O_{32}$
2#	1316	CaF_2
	1216	CaF_2 + $Ca_{12}Al_{14}F_2O_{32}$
	998	CaF_2 + $Ca_{12}Al_{14}F_2O_{32}$ + $MgAl_2O_4$
3#	1264	CaF_2
	1231	CaF_2 + $Ca_{12}Al_{14}O_{33}$
	972	CaF_2 + $Ca_{12}Al_{14}O_{33}$ + $MgAl_2O_4$ + $Ca_5(BO_3)_3F$
4#	1230	CaF_2
	1186	CaF_2 + $CaAl_4O_7$
	868	CaF_2 + $CaAl_4O_7$ + $MgAl_2O_4$ + $Ca_5(BO_3)_3F$

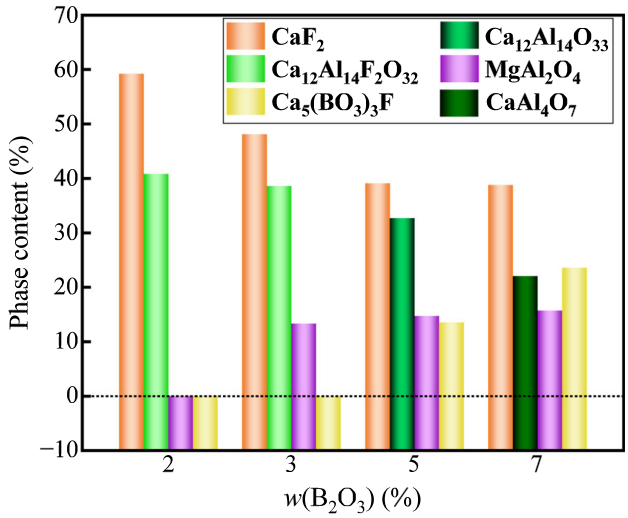

Fig. 4—The content of phases in the slags with various B_2O_3 contents.

The *K*-value method was used to semi-quantitatively analyze the phase content of the quenched slags with different B_2O_3 contents from 2 to 7 mass pct, as shown in Figure 4. Although this method can only calculate the phase content in the slag semi-quantitatively, it can determine the approximate proportion of the phase in the slag.[42,43] As shown in Figure 4, CaF_2 occupies a significant proportion of the phase content in the slags, which indicated that CaF_2 was the dominant crystalline phase. With the increase of B_2O_3 in the slag, the content of CaF_2 phase decreased, while the content of $MgAl_2O_4$ phase and $Ca_5(BO_3)_3F$ phase increased. Furthermore, the amount of crystalline phase represented by P2 seems to be decreasing. The change in phase content may be due to formation of $Ca_5(BO_3)_3F$.

C. *Morphologies of Crystalline Phases*

The four experimental molten slags were quenched at 600 °C (873 K) with a cooling rate of 15 °C·min^{-1} and subsequently analyzed by SEM–EDS. Quenching at lower temperature is beneficial to the full precipitation of crystalline phase. The morphologies of crystalline phases and the elemental mappings of the current slags are depicted in Figures 5, 6, 7, and 8. A comparison of SEM–EDS and XRD results indicates that the dominant crystalline phase was CaF_2 in ESR-type CaF_2–CaO–Al_2O_3–MgO slags with varying B_2O_3 content from 2 to 7 mass pct.

The SEM–EDS analysis of quenching slag 1# is presented in Figure 5. The spherical CaF_2 was the predominant crystalline phase, which accounted for the largest proportion. The results of EDS 2 in Figure 5 show that the atomic ratio of Ca, Al, O and F elements is close to that of $Ca_{12}Al_{14}F_2O_{32}$, which proves the existence of $Ca_{12}Al_{14}F_2O_{32}$. So reticulate $Ca_{12}Al_{14}F_2O_{32}$ was observed between the interstitial spaces of CaF_2. Due to the low concentration of Mg elements, $MgAl_2O_4$ was not detected. This aligns with the absence of $MgAl_2O_4$ in the XRD analysis. The SEM–EDS analysis is consistent with the XRD result (as depicted in Figure 3(a)).

The SEM–EDS analysis of quenching slag 2# as seen in Figure 6, the spherical CaF_2 remains the dominant crystalline phase. Differently, there is a notable transformation in the morphology of $Ca_{12}Al_{14}F_2O_{32}$, which has transitioned into a dendritic structure, and its concentration has further decreased. Additionally, there is an accumulation of Mg element, resulting in the detection of dot-like $MgAl_2O_4$. These observations from the SEM–EDS analysis align with the XRD results (Figure 3(b)).

The SEM–EDS analysis of quenching slag 3# is presented in Figure 7. It was evident from the figure that the spherical CaF_2 transitioned into faceted. Additionally, $Ca_{12}Al_{14}F_2O_{32}$ was significantly reduced, while long strip-shaped $Ca_{12}Al_{14}O_{33}$ was detected. Furthermore, block-like $MgAl_2O_4$ and MgO were detected in slag 3#.

The SEM–EDS analysis of quenching slag 4# is illustrated in Figure 8. It is clear from the Figure 8 that a limited amount of CaF_2 were detected. Then a significant amount of face-like $CaAl_4O_7$ were observed. There was a slight increase in the content of block-like $MgAl_2O_4$. Interestingly, different from the XRD analysis of slag 4# (Figure 3(d)), the SEM–EDS analysis did not detect $Ca_5(BO_3)_3F$. This discrepancy may arise from the small atomic radius of B, which makes it challenging to detect by SEM–EDS.[44] However, the EDS analysis

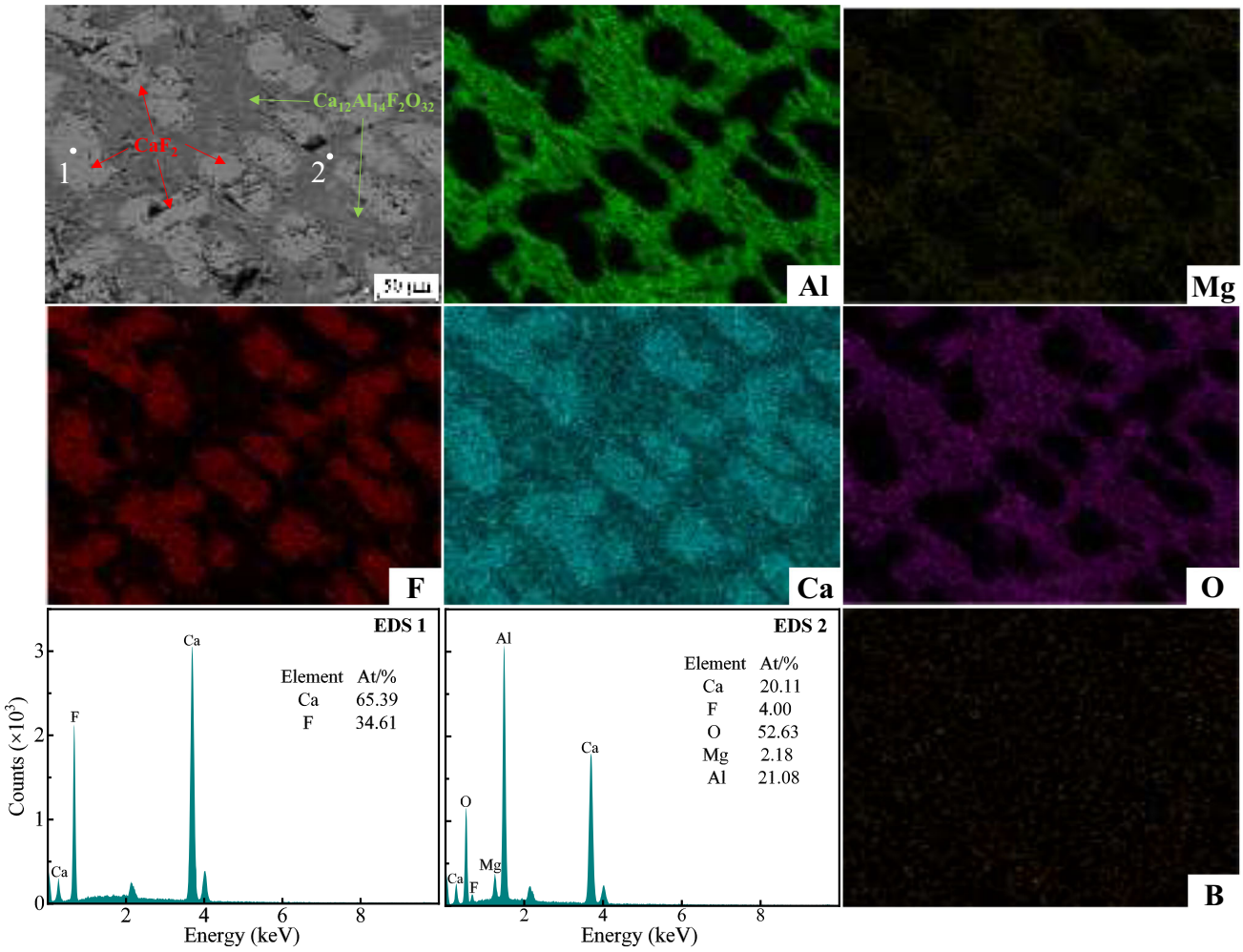

Fig. 5—SEM–EDS analysis of quenching slag 1# containing 2 mass pct B_2O_3.

of point 4 in Figure 8 showed that the atomic ratio of Ca, O, and F was very close to that of $Ca_5(BO_3)_3F$ phase.

In summary, an increase in B_2O_3 content in the slag leads to a decrease in the crystallization amounts of CaF_2 and $Ca_{12}Al_{14}F_2O_{32}$, accompanied by the formation of $Ca_{12}Al_{14}O_{33}$ phase (in slag 3#) or $CaAl_4O_7$ (in slag 4#). The morphology of the dominated phase CaF_2 is transformed from ellipsoidal to faceted.

D. *Phase Equilibrium Calculations*

The phase equilibrium of the slags during cooling was calculated by FactSage 8.2, and the results are given in Figure 9. As depicted in Figures 9(a) through (c), the sequence of crystal precipitation of the four slags investigated during the cooling was as follows: $CaF_2 \rightarrow Ca_{12}Al_{14}F_2O_{32} \rightarrow MgAl_2O_4$ (and MgO for slag 1#) $\rightarrow Ca_3B_2O_6$. Notably, increasing B_2O_3 content decreases the crystallization amount of $Ca_{12}Al_{14}F_2O_{32}$ in the slag from 38 to 21 pct. Furthermore, $Ca_{12}Al_{14}F_2O_{32}$ does not crystallize in slag 4# at 971°C.

From Figure 9(a), $MgAl_2O_4$ phase and MgO phase were found in the calculation result of slag 1#, but they were not found in the XRD result of slag 1#. Figure 9(c) and (d) illustrates the phase equilibrium calculation results for slags 3# and 4# during cooling. Interestingly, $Ca_{12}Al_{14}O_{33}$ and $CaAl_4O_7$ are absent in Figures 9(c) and (d), which differ from the XRD and SEM–EDS analysis of the slags. Additionally, instead of $Ca_5(BO_3)_3F$, the calculation results suggest the presence of $Ca_3B_2O_6$ crystalline phases. The deviation may be since FactSage predictions only provide results in the thermodynamic equilibrium state, whereas the slag state is often affected by kinetic conditions in practice. Additionally, Huang *et al.*[16] reveal that $[BO_4]$ structure units increased with B_2O_3 addition in CaF_2–CaO–Al_2O_3-based slags and caused an increase in component diffusion resistance. Similarly, when the amount of B_2O_3 added exceeded a critical value (a certain value in the range of 5 to 7 mass pct), CaF_2 and CaO in the slag may be more inclined to combine with B_2O_3 to form $Ca_5(BO_3)_3F$ in this study. This discrepancy may also arise from the FactSage calculation not involving the reaction caused by CaF_2

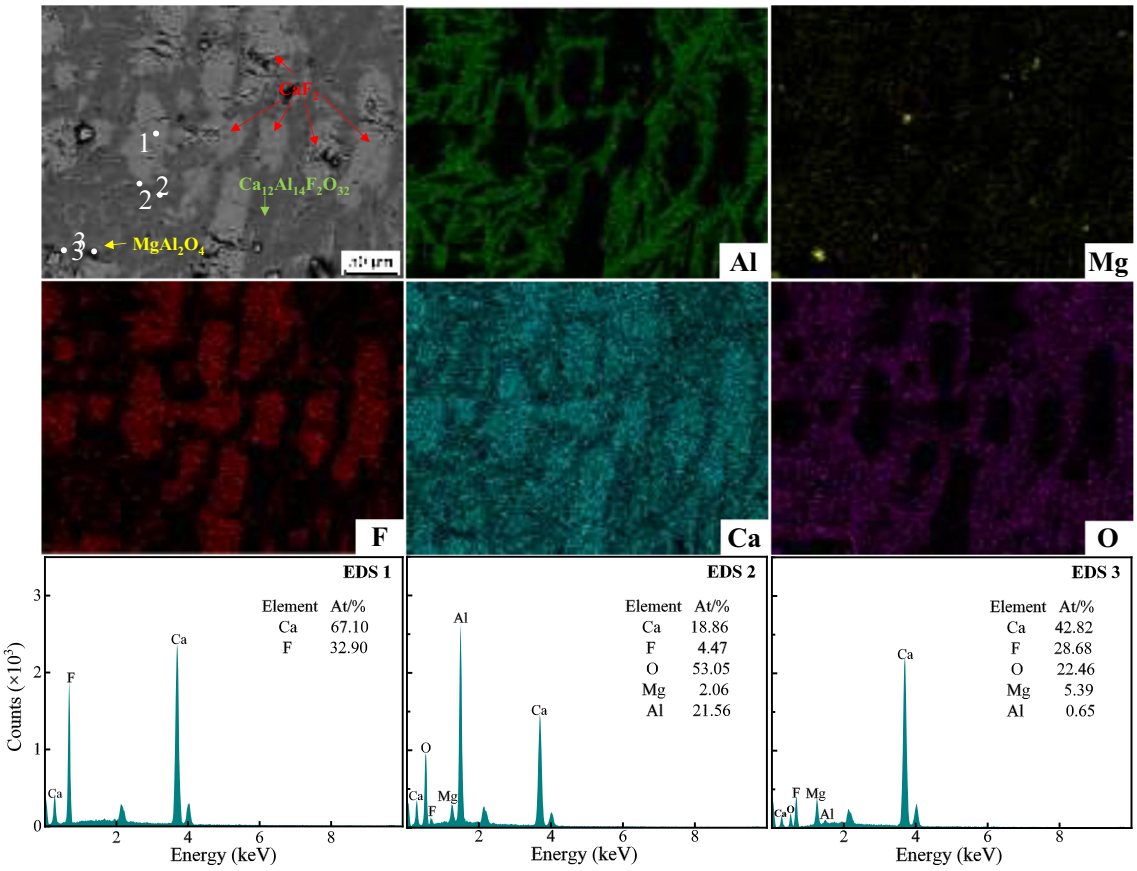

Fig. 6—SEM–EDS analysis of quenching slag 2# containing 3 mass pct B_2O_3.

diffusion. Besides, it is worth noting that Kozhaya *et al.*[45] have also found that the CaF_2–CaO–B_2O_3 slag would undergo peritectic reaction (2) to from $Ca_5(BO_3)_3F$. This further proves the above reaction process. Therefore, the content of CaF_2 and $Ca_{12}Al_{14}F_2O_{32}$ decreases when the content of $Ca_5(BO_3)_3F$ increases in the slags. The relevant thermodynamic calculations cannot be provided due to the lack of thermodynamic data of $Ca_5(BO_3)_3F$, but it will be further explored in subsequent studies.

$$Ca_5(BO_3)_3F = \text{Liq.} + CaO + Ca_3(BO_3)_2. \qquad [2]$$

E. *Crystallization Time of Crystalline Phases*

The XRD and SEM–EDS analyses demonstrate that the first-crystalline phase (CaF_2) was the dominated crystalline phase, which significantly affects the crystallization behaviors of the B_2O_3-bearing ESR slag. Therefore, the crystallization kinetics analysis of CaF_2 phase was performed. The relative crystallinity of CaF_2 phase in the slags 1# to 4# is shown in Figure 10. The slope of the curve signifies the crystallization rate of the initial crystalline phases. It was evident that the crystallization rate initially increased, reached a maximum at around 50 pct relative crystallinity, and then decreased during the cooling process. Moreover, from Figure 10, the crystallization process of CaF_2 carried out only for a short time at higher cooling rate (except slag 4#). Fan *et al.*[46] suggested that crystallization consists of both nucleation and crystal growth processes. Therefore, the increasing cooling rate will decrease the incubation time and inhibit the crystallization ability of the slag. And it should be noted that the nucleation process will be totally suppressed once the cooling rate exceeds the critical cooling rate.[30] On the contrary, the crystallization time of CaF_2 for slag 4# is significantly higher than that of other slags. It can be seen from Figure 1(d) that P1 and P2 overlap on the DSC curve, which suggested $CaAl_4O_7$ crystal began to crystallize at the end of the crystallization of CaF_2 crystal at 25°C·min^{-1}. As a result, the relative crystallinity of CaF_2 crystal in slag 4# is seriously disturbed by crystallization of $CaAl_4O_7$ at the crystallization rate of 25 °C·min^{-1}. This is the reason why slag 4# is different from others, while the crystallization time of the CaF_2 phase in slag 4# does not increase significantly at the cooling rate of 15 °C·min^{-1} due to sufficient incubation time.

The time for 50 pct crystallization of CaF_2 phase is shown in Figure 11. As observed, the crystallization time increased first and then decreased with the increasing B_2O_3 in the slag at the cooling rate of 15 °C·min^{-1}. From the XRD of slag 3# (as shown in Figure 3(c)), it was found that $Ca_5(BO_3)_3F$ would precipitate.

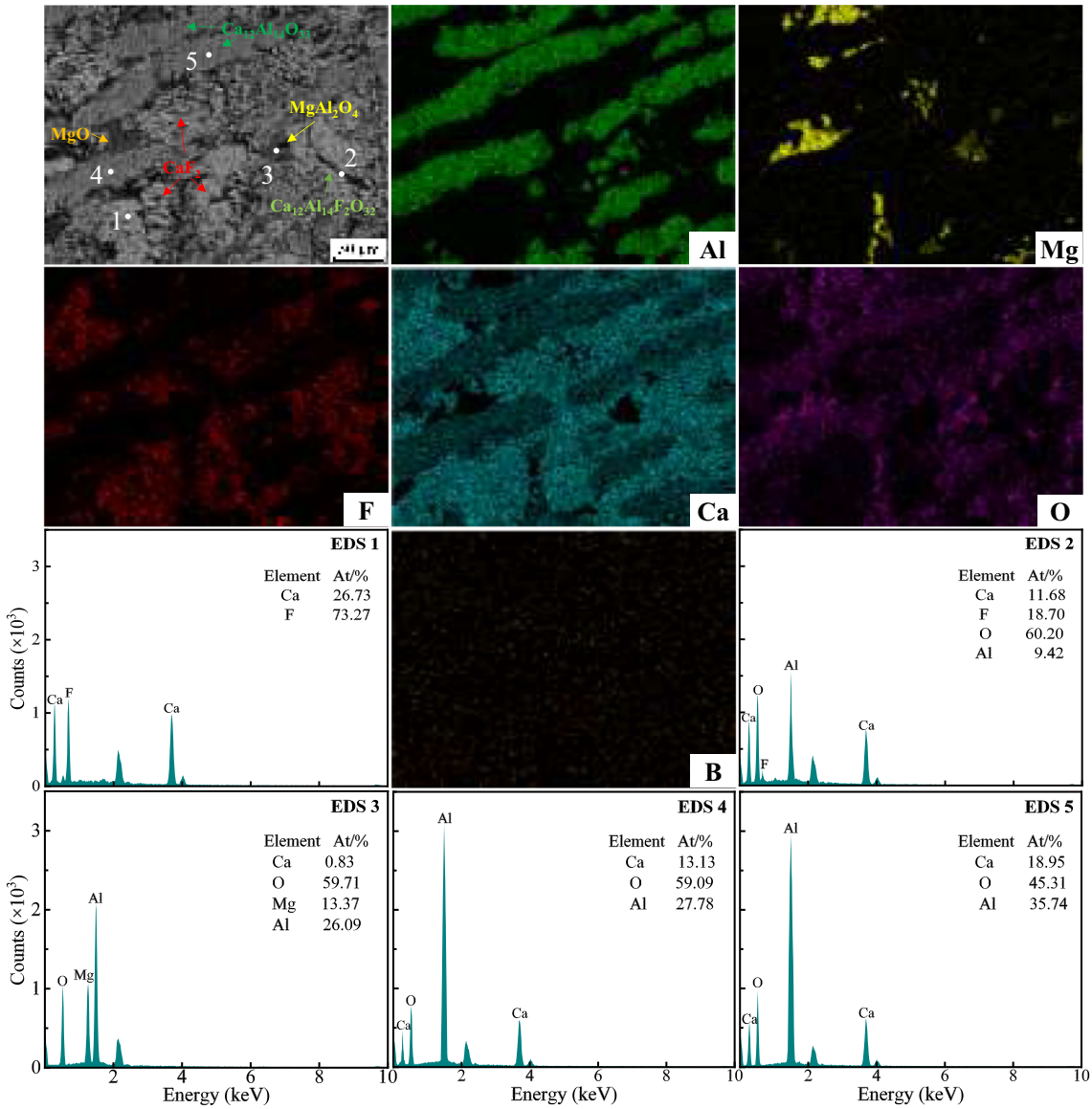

Fig. 7—SEM–EDS analysis of quenching slag 3# containing 5 mass pct B_2O_3.

Therefore, the binding force between B_2O_3 and CaF_2 would be enhanced, which undoubtedly increased the crystallization resistance of CaF_2 crystal in melt slag. Therefore, the crystallization time of CaF_2 crystal increased as B_2O_3 addition increased. However, the crystallization amount of CaF_2 crystal decreased significantly in the slag 4# from the SEM analysis (as depicted in Figure 8), which resulted the reduction of crystallization time of the CaF_2 crystal.

During the cooling process of slags 1# to 4#, a large amount of CaF_2 undergoes crystallization, resulting in the formation of a solid layer of slag film. The precipitation of CaF_2 improves the electrical conductivity of solid layer and leads to an increase in current loss form the mold.[47] This triggers an elevation in the temperature of the slag near the mold wall, enhances the heat driving force, and increases the radial heat loss of slag pool. Furthermore, the crystallization of CaF_2 is unfavorable to provide appropriate horizontal heat transfer which is one of the main factors for surface defects and unstable ESR operation.[17] To inhibit the crystallization of CaF_2 crystals, it is recommended to increase the B_2O_3 content in the slag.

IV. CONCLUSION

The crystallization behaviors of CaF_2–CaO–Al_2O_3–MgO–B_2O_3 slags were studied by DSC, XRD, SEM–EDS, and FactSage 8.2. The conclusions are summarized as follows:

(1) The CaF_2–CaO–Al_2O_3 slag with a small amount of MgO and B_2O_3 addition would exhibit three or four crystallization events during cooling process. In

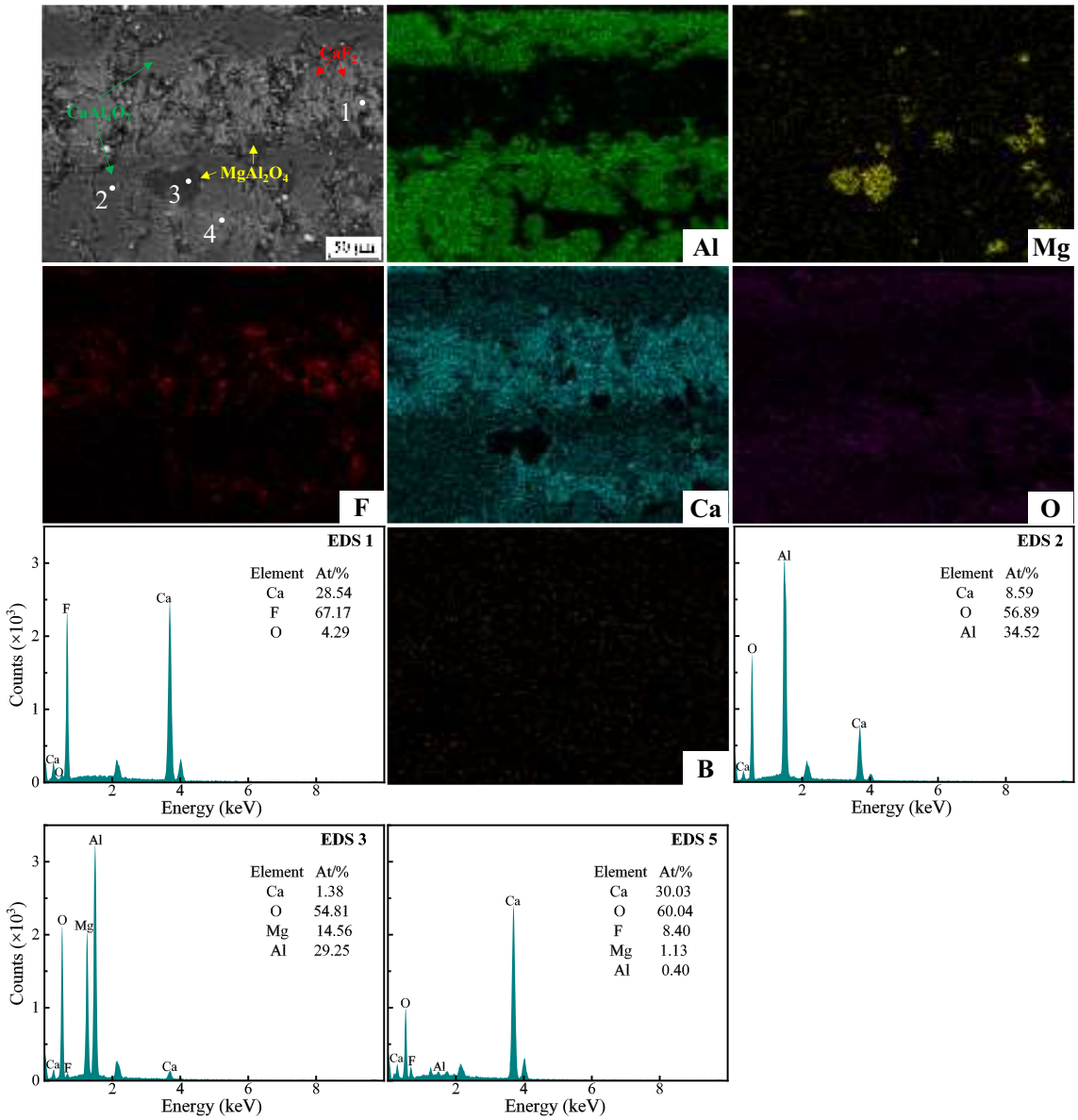

Fig. 8—SEM–EDS analysis of quenching slag 4# containing 7 mass pct B_2O_3.

addition, the increase of B_2O_3 content suppresses the crystallization tendency of CaF_2–CaO–Al_2O_3–MgO slag and decreases the crystallization temperature of crystallization phases.

(2) The addition of B_2O_3 could significantly change the crystallization sequence of the CaF_2–CaO–Al_2O_3–MgO–B_2O_3 slag. In the slag with 2 mass pct B_2O_3, the crystallization sequence is $CaF_2 \rightarrow Ca_{12}Al_{14}F_2O_{32}$. The crystallization sequence is $CaF_2 \rightarrow Ca_{12}Al_{14}O_{33} \rightarrow MgAl_2O_4 + Ca_5(BO_3)_3F$ in the slag with 5 mass pct B_2O_3, while in the slag containing 7 mass pct B_2O_3, the crystallization sequence is $CaF_2 \rightarrow CaAl_4O_7 \rightarrow MgAl_2O_4 + Ca_5(BO_3)_3F$.

(3) The morphology of the crystalline phases undergoes noticeable changes as the B_2O_3 content increases from 2 to 7 mass pct. The spherical CaF_2 transforms

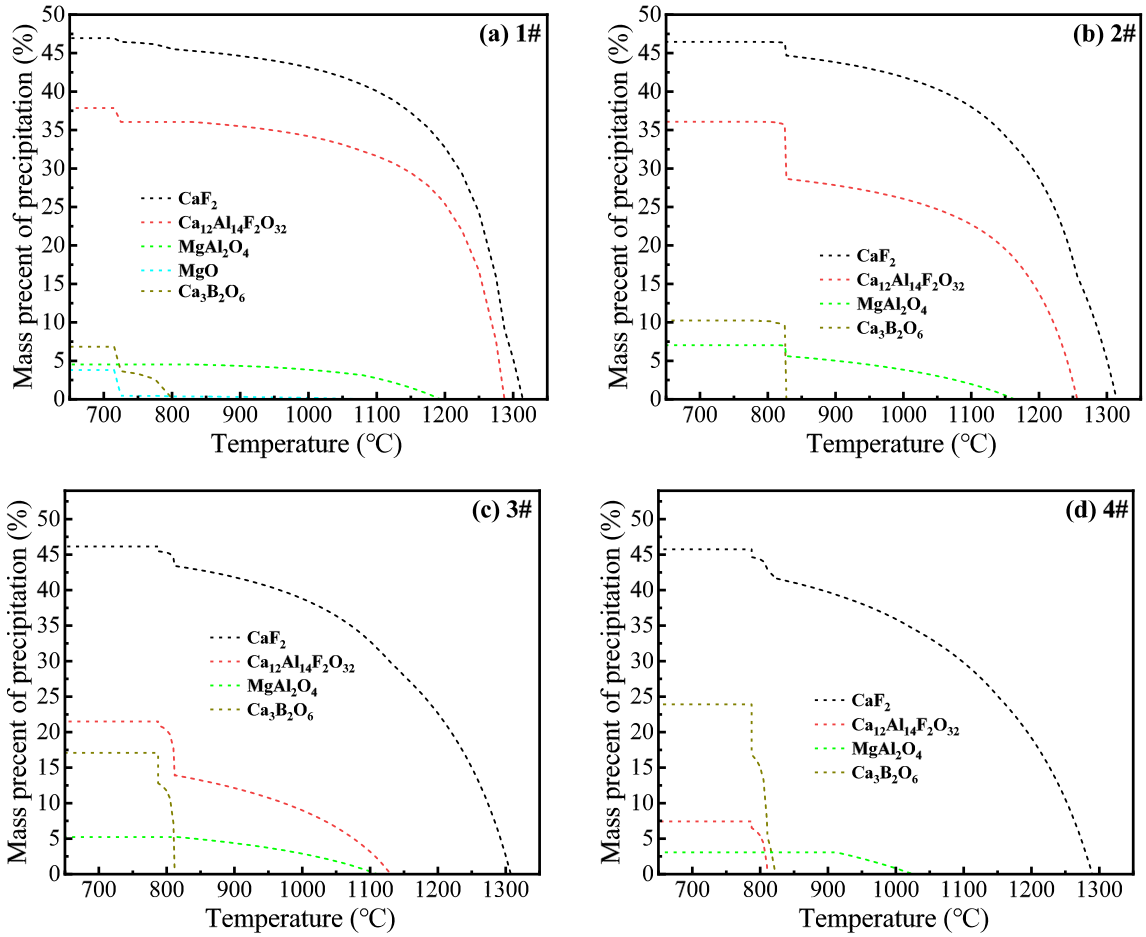

Fig. 9—The mass percent of crystalline phases for the slags during cooling: (*a*) slag 1#: $w(B_2O_3)$ = 2 mass pct, (*b*) slag 2#: $w(B_2O_3)$ = 3 mass pct, (*c*) slag 3#: $w(B_2O_3)$ = 5 mass pct, and (*d*) slag 4#: $w(B_2O_3)$ = 7 mass pct.

into face like. While the reticulate $Ca_{12}Al_{14}F_2O_{32}$ evolves into dendritic shapes until it eventually diminishes. Simultaneously, the appearance of calcium aluminate ($Ca_{12}Al_{14}O_{33}$ or $CaAl_4O_7$) becomes evident. $MgAl_2O_4$ transitions from dot-like to a block-like form, but the crystalline amount is low. Notably, the first-crystalline phase CaF_2 is the main crystalline phase in the slag with varying B_2O_3 content from 2 to 7 mass pct.

(4) The crystallization time increased first and then decreased with increasing B_2O_3 addition in the CaF_2–CaO–Al_2O_3–MgO slag at a cooling rate of 15 °C·min^{-1}. Moreover, B_2O_3 addition inhibits the crystallization of the dominant phase CaF_2, which improving the lubrication and heat transfer performance of ESR-type CaF_2–CaO–Al_2O_3–MgO slags.

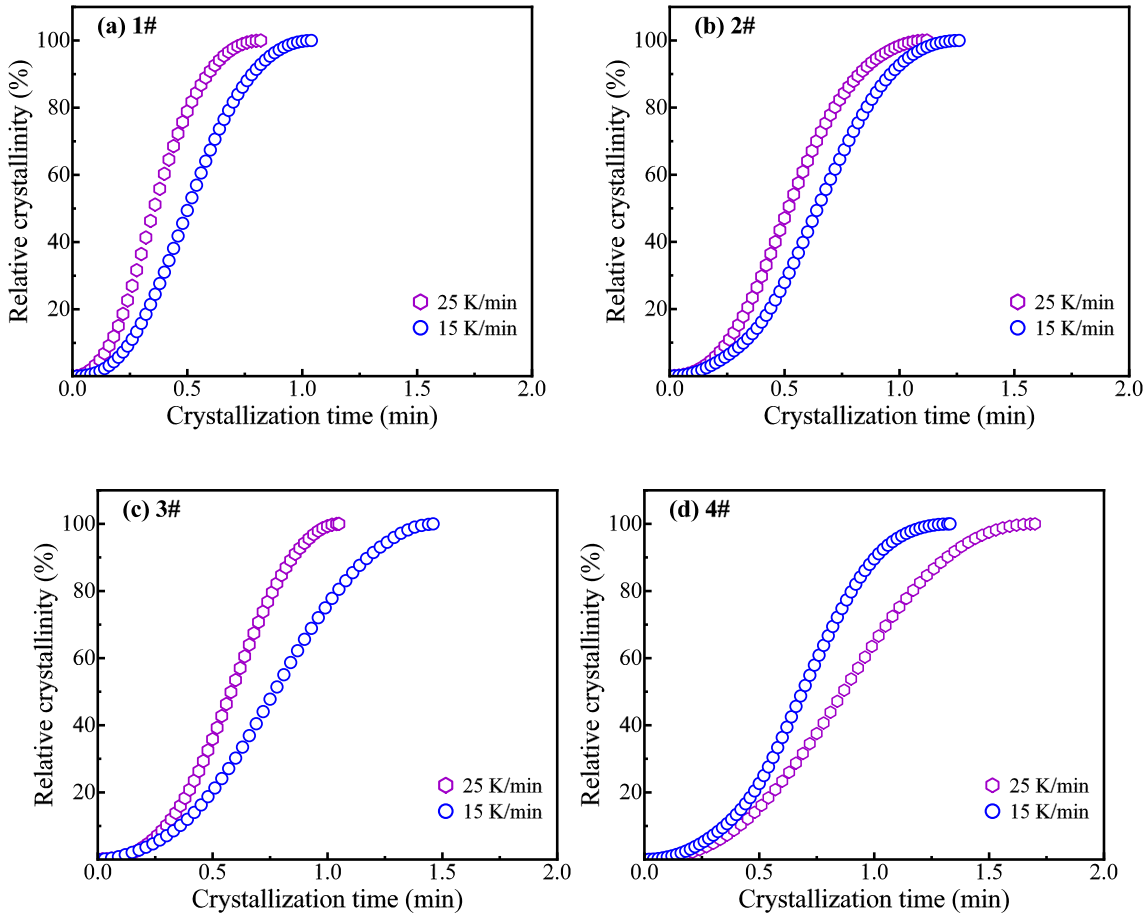

Fig. 10—The relative crystallinity of the CaF_2 phase in the slag changes with time: (*a*) slag 1#: $w(B_2O_3)$ = 2 mass pct, (*b*) slag 2#: $w(B_2O_3)$ = 3 mass pct, (*c*) slag 3#: $w(B_2O_3)$ = 5 mass pct, and (*d*) slag 4#: $w(B_2O_3)$ = 7 mass pct.

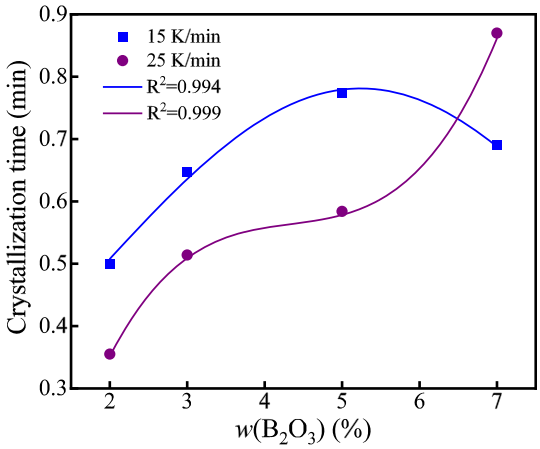

Fig. 11—The crystallization time for 50 pct crystallinity of the first-crystalline phase.

ACKNOWLEDGMENTS

This project is supported by the National Natural Science Foundation of China (Grant Nos. 52174317, 52274337 and U1960203).

CONFLICT OF INTEREST

On behalf of all authors, the corresponding author states that there is no conflict of interest.

SUPPLEMENTARY INFORMATION

The online version contains supplementary material available at https://doi.org/10.1007/s11663-024-03243-7.

REFERENCES

1. M. Tong, X. Di, C. Li, and D. Wang: *Mater. Charact.*, 2018, vol. 144, pp. 631–40.
2. J. Jiang, H. Wu, J. Liang, and D. Tang: *Mater. Sci. Eng. A*, 2013, vol. 587, pp. 359–64.
3. X.M. Zang, T.Y. Qiu, W.M. Li, X. Deng, Z.H. Jiang, and H. Song: *J. Iron. Steel Res. Int.*, 2016, vol. 23, pp. 297–304.
4. M. El-Shennawy, A. Farahat, M. Masoud, and A. Abdel-Aziz: *Int. J. Mech. Eng. Educ.*, 2016, vol. 5, pp. 1–14.
5. S.N. Ghali, H.S. El-Faramawy, and M.M. Eissa: *J. Miner. Mater. Charact. Eng.*, 2012, vol. 11, pp. 995–99.
6. S.C. Duan, X. Shi, F. Wang, M.C. Zhang, Y. Sun, H.J. Guo, and J. Guo: *Metall. Mater. Trans. B*, 2019, vol. 50B, pp. 3055–71.
7. L. Peng, Z. Jiang, and X. Geng: *Metals*, 2019, vol. 9, p. 1300.
8. X. Xing, Z. Pang, C. Mo, S. Wang, and J. Ju: *J. Non-Cryst. Solids*, 2020, vol. 530, p. 119801.
9. S. Esfahani and M. Barati: *J. Non-Cryst. Solids*, 2016, vol. 436, pp. 35–43.
10. W. Wang, S. Dai, T. Zhang, H. Zhang, Z. Li, and Y. Xie: *J. Clean. Prod.*, 2021, vol. 288, p. 125603.
11. J. Cho, H. Shibata, T. Emi, and M. Suzuki: *ISIJ Int.*, 1998, vol. 38, pp. 440–46.
12. C.B. Shi, J. Li, J.W. Cho, F. Jiang, and I.H. Jung: *Metall. Mater. Trans. B*, 2015, vol. 46B, pp. 2110–20.
13. Y. Liu, Y. Wang, G. Li, C. Yuan, R. Lu, and B. Li: *J. Therm. Anal. Calorim.*, 2019, vol. 139, pp. 923–31.
14. D. Zheng, J. Li, C. Shi, and J. Ju: *Metall. Mater. Trans. B*, 2019, vol. 50B, pp. 1148–60.
15. J.T. Ju, J.L. An, and G.H. Ji: *J. Min. Metall. B*, 2019, vol. 55, pp. 397–404.
16. Y. Huang, C.B. Shi, X.X. Wan, J.L. Li, D.L. Zheng, and J. Li: *J. Iron. Steel Res. Int.*, 2021, vol. 28, pp. 1530–40.
17. L. Peng, Z. Jiang, X. Geng, F. Liu, and H. Li: *Metals*, 2019, vol. 9, p. 1331.
18. C.B. Shi, D.L. Zheng, S.H. Shin, J. Li, and J.W. Cho: *Int. J. Miner. Metall. Mater.*, 2017, vol. 24, pp. 18–24.
19. Y.J. Zhang, L.Z. Kong, X.M. Zang, and S.S. Li: *High Temp. Mater. Process. (Lond.)*, 2024, vol. 43, p. 20220316.
20. C.B. Shi, M.D. Seo, J.W. Cho, and S.H. Kim: *Metall. Mater. Trans. B*, 2014, vol. 45B, pp. 1081–97.
21. D. Durinck, P.T. Jones, B. Blanpain, P. Wollants, G. Mertens, and J. Elsen: *J. Am. Ceram. Soc.*, 2007, vol. 90, pp. 1177–85.
22. E. Kozeschnik, W. Rindler, and B. Buchmayr: *Int. J. Mater. Res.*, 2007, vol. 98, pp. 826–31.
23. Q. Chen and B. Sundman: *Mater. Trans.*, 2002, vol. 43, pp. 551–59.
24. E. Balitchev, H. Meuser, D. Neuschütz, and W. Bleck: *Steel Res. Int.*, 2004, vol. 75, pp. 13–19.
25. L.B. Otani, J. Soyama, G. Zepon, A. Costa e Silva, C.S. Kiminami, W.J. Botta, and C. Bolfarini: *J. Phase Equilib. Diffus.*, 2017, vol. 38, pp. 298–304.
26. D. Zheng, C. Shi, J. Li, and J. Ju: *ISIJ Int.*, 2020, vol. 60, pp. 492–98.
27. C.B. Shi, M.D. Seo, H. Wang, J.W. Cho, and S.H. Kim: *Metall. Mater. Trans. B*, 2014, vol. 46B, pp. 345–56.
28. M.D. Seo, C.B. Shi, J.Y. Baek, J.W. Cho, and S.H. Kim: *Metall. Mater. Trans. B*, 2015, vol. 46B, pp. 2374–83.
29. B. Ding, Q. Liao, X. Zhu, and H. Wang: *Appl. Therm. Eng.*, 2021, vol. 184, p. 116260.
30. C.B. Shi, M.D. Seo, H. Wang, J.W. Cho, and S.H. Kim: *Metall. Mater. Trans. B*, 2015, vol. 46B, pp. 345–56.
31. B. Lin, H. Wang, X. Zhu, Q. Liao, and B. Ding: *Appl. Therm. Eng.*, 2016, vol. 96, pp. 432–40.
32. J. Wei, W. Wang, L. Zhou, D. Huang, H. Zhao, and F. Ma: *Metall. Mater. Trans. B*, 2013, vol. 45B, pp. 643–52.
33. H. Nakada, M. Susa, Y. Seko, M. Hayashi, and K. Nagata: *ISIJ Int.*, 2008, vol. 48, pp. 446–53.
34. A. Mitchell and K. Kelkar: *Ironmak. Steelmak.*, 2021, vol. 48, pp. 1151–57.
35. P. Hu, X. Wang, J. Wei, M. Yao, and Q. Guo: *ISIJ Int.*, 2018, vol. 58, pp. 892–98.
36. C. Yang, G. Wen, Q. Sun, and P. Tang: *Metall. Mater. Trans. B*, 2017, vol. 48B, pp. 1292–1307.
37. X. Wang, L. Kong, M. Yao, and X. Zhang: *Metall. Mater. Trans. B*, 2017, vol. 48B, pp. 357–66.
38. S. Zhang, Q. Wang, S. He, and Q. Wang: *Metall. Mater. Trans. B*, 2018, vol. 49B, pp. 2038–49.
39. J. Yu, F. Liu, Z. Jiang, C. Kang, K. Chen, H. Li, and X. Geng: *Steel Res. Int.*, 2018, vol. 89, p. 1700481.
40. A. Plotkowski and M. Krane: *Int. J. Heat Mass Transf.*, 2016, vol. 100, pp. 11–23.
41. H. Khan, A.S. Yerramilli, A. D'Oliveira, T.L. Alford, D.C. Boffito, and G.S. Patience: *Can. J. Chem. Eng.*, 2020, vol. 98, pp. 1255–66.
42. Y. Chen, L. Zhang, J. Zhang, P. Liu, T. Zhou, H. Zhang, D. Gong, D. Tang, and D. Shen: *Opt. Mater.*, 2015, vol. 50, pp. 36–39.
43. H. Wang, B. Ding, X. Zhu, Y. Tan, X.-Y. He, and Q. Liao: *Int. J. Heat Mass Transf.*, 2017, vol. 113, pp. 286–94.
44. Y. Kashiwaya, T. Nakauchi, K.S. Pham, S. Akiyama, and K. Ishii: *ISIJ Int.*, 2007, vol. 47, pp. 44–52.
45. N. Kozhaya, M. Ferriol, M. Cochez, and M. Aillerie: *XXXVII JEEP—37th Conference on Phase Equilibria*, Saint-Avold, 2011.
46. Y. Fan, E. Shibata, A. Iizuka, and T. Nakamura: *Metall. Mater. Trans. B*, 2015, vol. 46B, pp. 2158–64.
47. X. Huang, Z. Liu, Y. Duan, C. Liu, and B. Li: *J. Mater. Res. Technol.*, 2022, vol. 20, pp. 3843–59.